Catalysis Letters (2022) 152:1029–1039
https://doi.org/10.1007/s10562-021-03700-x

Facile Synthesis of Fluorine Doped Rutile TiO_2 Nanorod Arrays for Photocatalytic Removal of Formaldehyde

Wenyu Diao[1] · **Jiayue Xu**[1] · **Xi Rao**[1] · **Yongping Zhang**[1]

Received: 31 March 2021 / Accepted: 31 May 2021 / Published online: 11 June 2021

Abstract

It is crucial to explore a facile synthesis of rutile TiO_2 nanorods anchored at carbon cloth at low temperature for applicable air purifier. Herein, antler-like TiO_2 rectangular bunched arrays were grown on carbon cloth by a hydrothermal method, and fluorine was doped into TiO_2 with solid diffusion of NH_4F at 300 °C. Fluorine doping induces oxygen vacancies in TiO_2, facilitating the charge transfer and providing more active sites for photocatalytic reactions. The F doped TiO_2 exhibits excellent photocatalytic oxidation of formaldehyde under UV and visible LED irradiation. UV–vis DRS and UPS results indicate that 3F-T@CC can harvest more visible light, and has the suitable energy band structure to generate hydroxyl radical and superoxide radical for the effective degradation of formaldehyde. EPR measurements prove the photogenerated superoxide radial ($\cdot O_2^-$) and hydroxyl radical ($\cdot OH$) are involved in oxidizing formaldehyde into CO_2 and H_2O.

Graphic Abstract

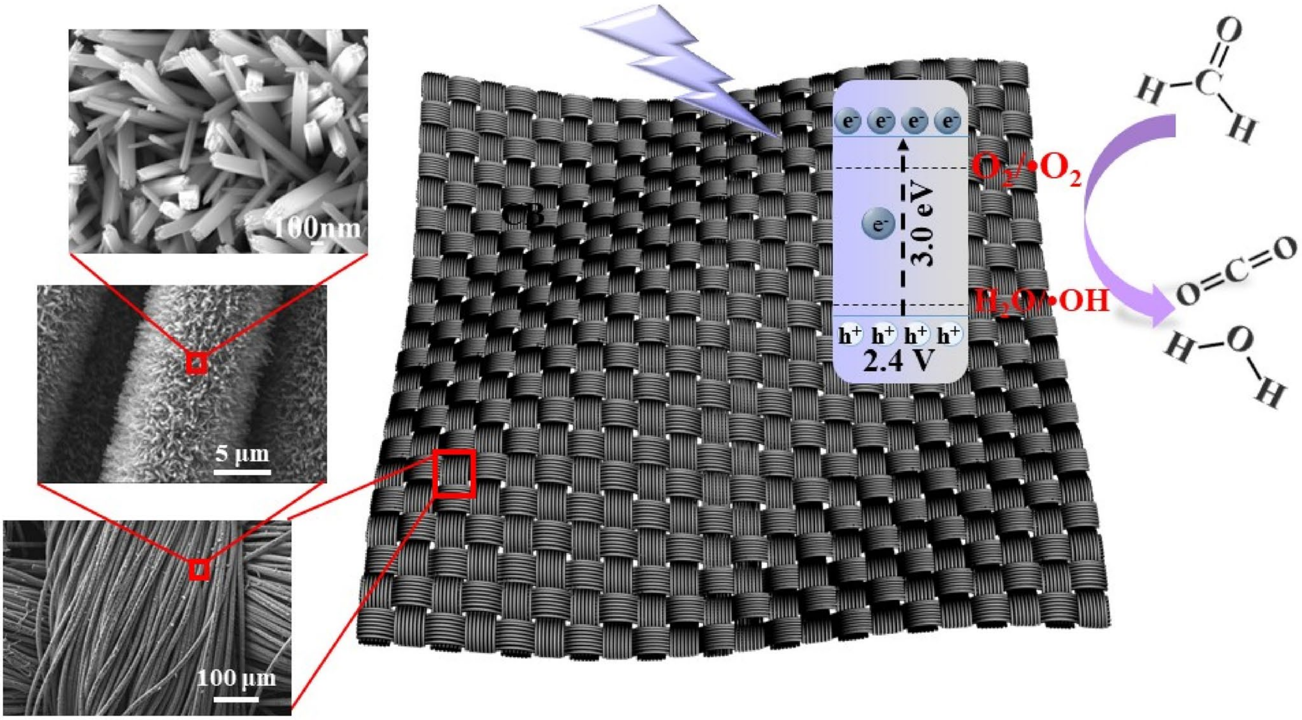

Photocatalytic degradation of formaldehyde by fluorine doped rutile TiO_2 nanorod arrays on carbon cloth.

Keywords Rutile TiO_2 · Photocatalysis · Formaldehyde · Photocatalysts · Nanorods

---

Extended author information available on the last page of the article

1 Introduction

Nowadays, volatile organic compounds (VOCs) have been becoming the main sources of the indoor air pollution, and its volatility and toxicity harm the human health, and deteriorate ecosystem as well. Among those VOCs, benzene, toluene and formaldehyde are perhaps the most pernicious to human health [1–4]. Formaldehyde is a highly toxic and suspicious carcinogen at low concentration presented in our living atmosphere. A large number of techniques have been employed to eliminate formaldehyde, such as adsorption [5, 6], plasma oxidation [7, 8], photocatalysis, [9–11] and photothermal catalysis [12, 13]. Photocatalysts have found extensive applications in photocatalytic viral disinfection, reduction of CO_2 and synthesis of organic compounds, effective contaminant removal [14–16]. Researches have found that photocatalysis is one of the most efficient and effective technique for photo-oxidation of formaldehyde, benzene, and toluene, with the advantages of green, pollution-free, mild conditions and reusability. Some commonly used semiconductor catalysts in photocatalytic oxidation of formaldehyde included TiO_2, $BiVO_4$, MnO_x, graphitic C_3N_4, [13–19] and TiO_2 has found widely application in VOCs degradation due to its stability, low cost and non-toxicity. However, its photocatalytic oxidation performance under visible light need to be improved further.

The light absorption performance of the catalyst has a great influence on the photocatalytic performance. Through the construction of heterojunction, dye sensitization and element doping, the optical absorption performance can be enhanced to improve the visible light response. As for the element doping, nonmetallic elements (such as F, Cl, Br, I, C and N) dopants can narrow the band gap of titanium dioxide [20–29]. Research found that fluorine doping makes the absorption edge of titanium dioxide red shift, enhances the visible light response, and makes titanium dioxide exhibiting higher activity in acetone photocatalytic oxidation under ultraviolet light, which means that the doping process is to tune the valence band and conduction band of titanium dioxide. However, those TiO_2 photocatalysts doped with fluorine were prepared by sol–gel synthesis, followed by calcination at high temperatures (500–700 °C) [24–29]. On the other hand, those photocatalysts are usually in the form of particles. TiO_2 nanorod arrays anchored on soft substrate were realized for flexible devices for energy harvesting [30]. Carbon cloth was used as soft substrate due to its high carrier transport performance and large specific surface area. And more importantly, nanorod arrays anchored on flexible substrate realized the immobilized integration catalysts for more conveniently gathering and recycling than powdery ones. Our recent study [31] realized the alkali metal (Na, K) and halogen (Cl) co-doped rutile TiO_2 arrays at 550 °C for efficient photocatalytic degradation of formaldehyde. It is therefore important to explore a simple method to prepare the TiO_2 arrays anchored on soft carbon cloth at low temperature for applicable utilization in air purifier.

Herein, soft carbon cloth was used as a substrate to anchor the TiO_2 nanorods for applicable air purifier, overcoming the shortcoming of powder diffusion by air flow. Rutile TiO_2 nanorod arrays were successfully grown on carbon cloth by a hydrothermal reaction of titanium butoxide and hydrochloric acid, and fluorine doped by solid diffusion of NH_4F at 300 °C. Fluorine element doping improves the photoelectric properties, increases the generation of oxygen vacancies, and improves the formaldehyde degradation performance.

2 Experimental Details

2.1 Preparation of Rutile TiO_2 Nanorod Arrays @ Carbon Cloth (CC)

Carbon cloth (CC) was used as soft substrate, immersed in a strong acid solution (H_2SO_4:$HNO_3 = 3:1$ by volume ratio) for 24 h, cleaned with deionized water by ultrasonic stirring, and dried at 80 °C. Titanium(IV) chloride (99.5%) and titanium(IV) butoxide ($Ti(OC_4H_9)_4$, 99%) were used as precursor for TiO_2, and ammonium fluoride (99.99%) for fluorine. 220 μL $TiCl_4$ was added into 10 mL 2.4 M hydrochloric acid, and then the dried CC was immersed in the above-mentioned solution for 12 h, then dried at 80 °C. The dried carbon cloth was heated at 400 °C for 30 min, forming TiO_2 nanoparticles coated on CC as the seed layer. 600 μL titanium butoxide (TNBT) was added drop by drop into 24 mL 6 M hydrochloric acid solution, stir the solution with ultrasonic stirring until clear solution was obtained. Carbon cloth was immersed into the solution, and transferred into an autoclave heated at 160 °C for 5.5 h. When cooled to room temperature, carbon cloth was taken out, cleaned with deionized water and ethanol, and dried at 80 °C to obtain the rutile TiO_2@CC.

TiO_2@CC was immersed into 25 mL NH_4F solution with certain concentration (NH_4F: $Ti(OC_4H_9)_4 = 0$, 2 wt%, 3 wt%, 4 wt%) for 24 h, dried, and heated at 300 °C for 2 h in air. The samples were cleaned with deionized water and ethanol, and dried at 80 °C, denoted as T@CC, 2F-T@CC, 3F-T@CC, 4F-T@CC, respectively. The F doped rutile TiO_2 arrays on CC was schematically illustrated in Scheme 1.

2.2 Characterization

The morphology and structure were examined by scanning electron microscopy (SEM, JSM-6610), transmission

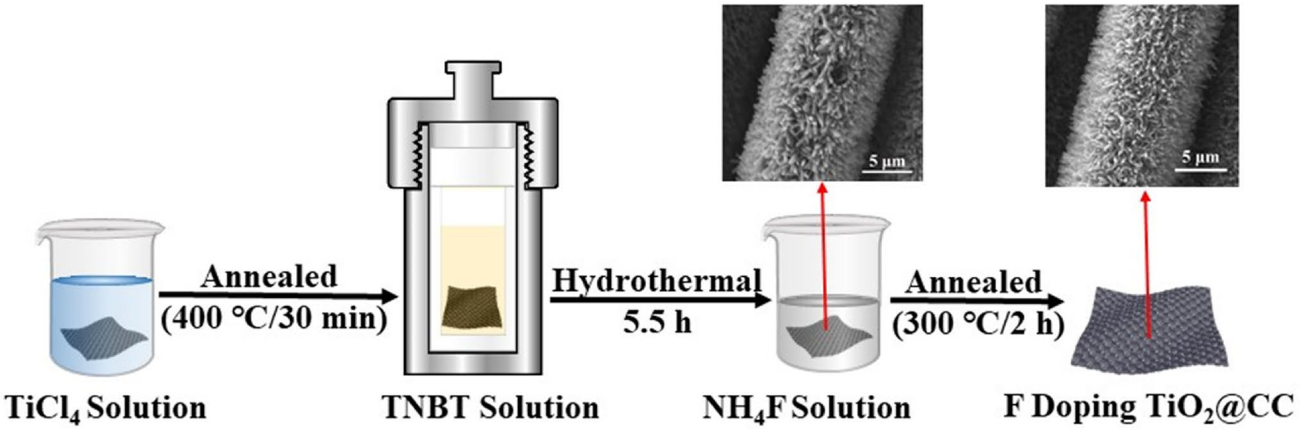

Scheme 1 Schematic illustration of the F doped rutile TiO_2 arrays on CC

electron microscopy (TEM, JEM-2100), X-ray diffraction (XRD, Shimadzu 7000) and Raman spectroscopy (LabRAM HR Evolution). X-ray photoelectron spectroscopy (XPS, Thermo Fisher ESCALAB 250Xi), and ultraviolet electron spectroscopy (UPS, He I $h\nu = 21.22$ eV) were used to investigate the core level and the valence states of the elements. Photocurrent response and electrochemical measurements were carried out on AutoLab workstation (PGSTAT 302N) using a 500 W Xe lamp ($\lambda \geq 365$ nm) as light source. The working electrode was made of 1×1 cm^2 sample sandwiched in FTO conductive glass, and the electrolyte was 0.25 M $NaSO_4$. UV–vis diffuse reflectance spectra (UV–vis DRS) were measured on Agilent Cary 5000 UV–vis NIR spectrometer with $BaSO_4$ as reference. Photoluminescence spectra (PL) were collected on Hitachi F-7000 spectrophotometer at room temperature. Free radical trapping experiments were carried out on electron paramagnetic resonance (EPR) spectrometer (Bruke, EMXnano) with 365 nm LED as excitation source.

2.3 Photocatalytic Removal of Formaldehyde

Formaldehyde gas removal was evaluated by a volatile organic compounds (VOCs) purification evaluation system (Suncat POV-18) at room temperature. The formaldehyde concentration was continuously monitored by formaldehyde sensors (DART sensor Co., Ltd.) at the inlet and outlet of the reactor. The 2 cm × 2 cm sample was evenly cut into three equal parts and put into a high transparent quartz tube with diameter of 6 mm. The flow rate of formaldehyde gas is strictly set at 50 mL/min, and the adsorption desorption balance is achieved before the degradation reaction. The formaldehyde concentration at the inlet is set at 0.5 mg/m^3. LED lamp (365 nm or 420 nm, 1.5 W) was used to irradiate the catalysts. The degradation rate of formaldehyde can be calculated according to the following equation:

$$\text{Degradation rate } \eta = \left(C_0 - C_t\right)/C_0 \times 100\% \qquad (1)$$

where C_0 is the concentration of HCHO at the inlet (CH1) after adsorption–desorption equilibrium, and C_t is the concentration of HCHO at the outlet (CH2) at time of t after irradiation.

3 Results and Discussion

The XRD pattern of T@CC (Fig. 1a) can be indexed with rutile phase TiO_2 (PDF no. 87–0710). After doping with fluorine, there appeared two weak diffraction peaks at 2θ of 38.1° and 48.2°, corresponding to the (004) and (200) crystal planes of anatase phase TiO_2 (PDF no. 73-1765), and its intensity increases with the increase of NH_4F amount during the annealing process. That shows that F doping promotes the growth of anatase TiO_2 during annealing at 300 °C, and fractional anatase phase TiO_2 may embed at the background of rutile phase. The Raman spectra (Fig. 1b) showed the characteristic peaks of rutile TiO_2, in which E_g and A_{1g} are located at 438.7 cm^{-1} and 610.4 cm^{-1}, respectively. The broad band at 281.5 cm^{-1} is due to the multi-photon scattering of rutile TiO_2, while a week peak at 185.5 cm^{-1} is attributed to anatase titania. After F doping, the peak of E_g shows slight blue shift and peak broadening, which is related to the formation of F–Ti–O. Some reports demonstrated that the E_g rutile mode showed red shift and attributed to nonstoichiometric effect and oxygen vacancies. However, the E_g mode in this study shows blue shift, and we attribute it to the formation of F–Ti–O bonds. The E_g mode was of the asymmetric bending of the O–Ti–O bonds in the {001} plane, caused by the opposite moving of the O atoms across the O–Ti–O bond [31–33]. The stronger F–Ti–O bonds suggested the Hook constant became larger, thus E_g mode shifted to higher wavenumber with F doping. Electron paramagnetic

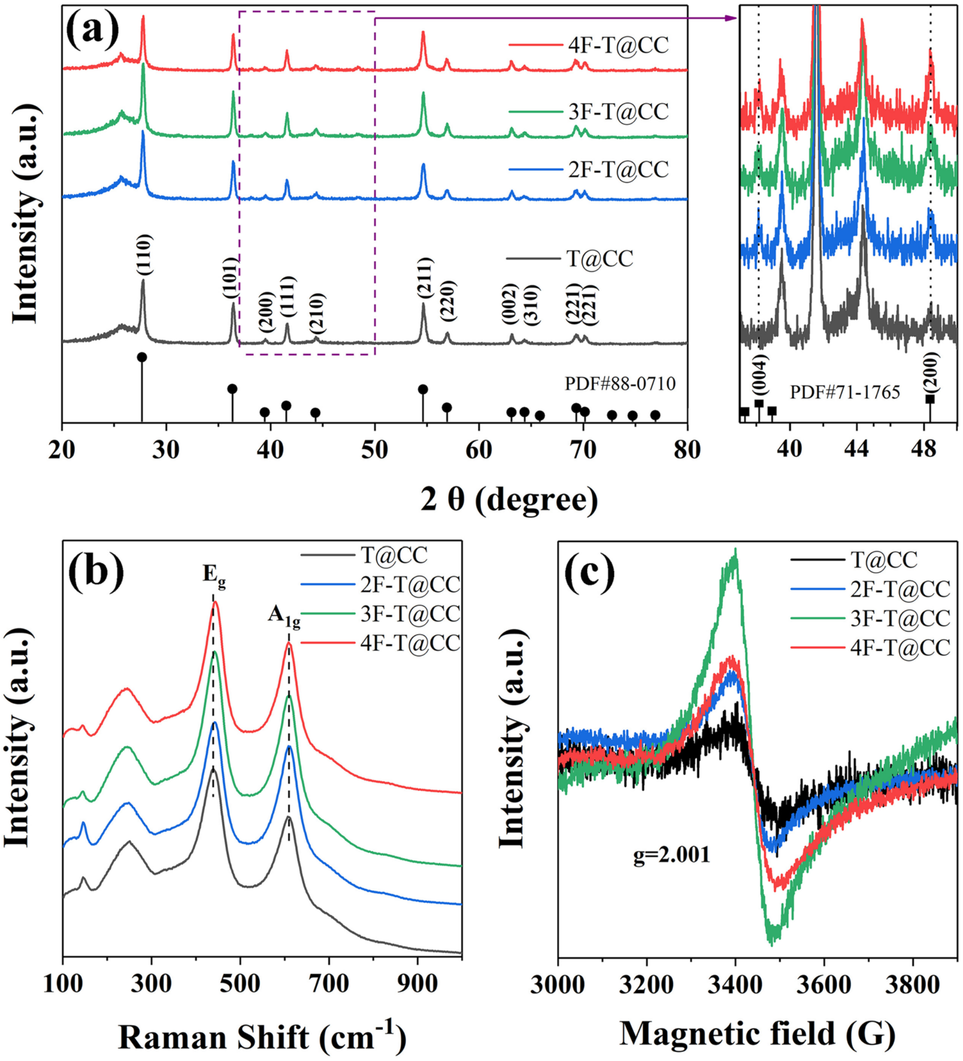

Fig. 1 XRD patterns (**a**), Raman spectroscopy (**b**) and EPR spectra (**c**) of T@CC, 2F-T@CC, 3F-T@CC, and 4F-T@CC

resonance (EPR) spectra (Fig. 1c) exhibit a resonance signal at g = 2.001, ascribed to the unpaired electrons trapped at the surface oxygen vacancies [31–34]. The signal intensity increased with the increase of fluorine doping, and 3FT@CC has the strongest signal. That strongly suggested that the fluorine doping induces oxygen vacancy in TiO_2.

SEM images (Fig. 2a–d) showed that TiO_2 nanorod arrays are densely covered the surface of the carbon fibers. The high magnitude SEM images (Figs. 2a'–d') showed the randomly aligned TiO_2 nanorods are about several micrometers in length and with square cross section with the side length of about 100 nm. The TiO_2 nanorod arrays appeared as antler-like rectangular columns spaced several micrometers [30]. The morphologies of TiO_2 nanorod arrays remain intact during the annealing process. Furthermore, the density of nanorods can be properly controlled by adjusting the concentration of the titanium (IV) butoxide in the hydrothermal process, providing more air contact area and reaction sites for formaldehyde degradation. The results showed that the nanoscale rutile TiO_2 nanorod arrays are successfully grown on carbon fibers.

TEM (Fig. 3a) image shows that there are folds and holes in the TiO_2 nanorods. The TiO_2 nanorods are rectangular columns bunches composed of smaller nanowires. For TEM analysis, the specimens were prepared by dissolving the nanorods in ethanol solution by ultrasonic stirring. TEM image shows some thin nanorods, disbundled from the rectangular bunched TiO_2. The selected area electron diffraction (SAED) pattern (Fig. 3b) confirms that the TiO_2 nanorods are crystalline rutile phase of TiO_2, consistent with XRD and Raman measurements. High resolution TEM (Fig. 3c) shows the lattice spacing is 0.325 nm, which corresponds to the rutile (101) crystal plane. The element mappings (Fig. 3d–g) show the homogeneous distribution of Ti, O and F on the TiO_2 nanorod arrays on carbon fiber. EDS results gave a semiquantitative element ratio of Ti:O:F is about 41.4%:57.6%:1.0%. The results show that F element is doped into rutile TiO_2 nanorods.

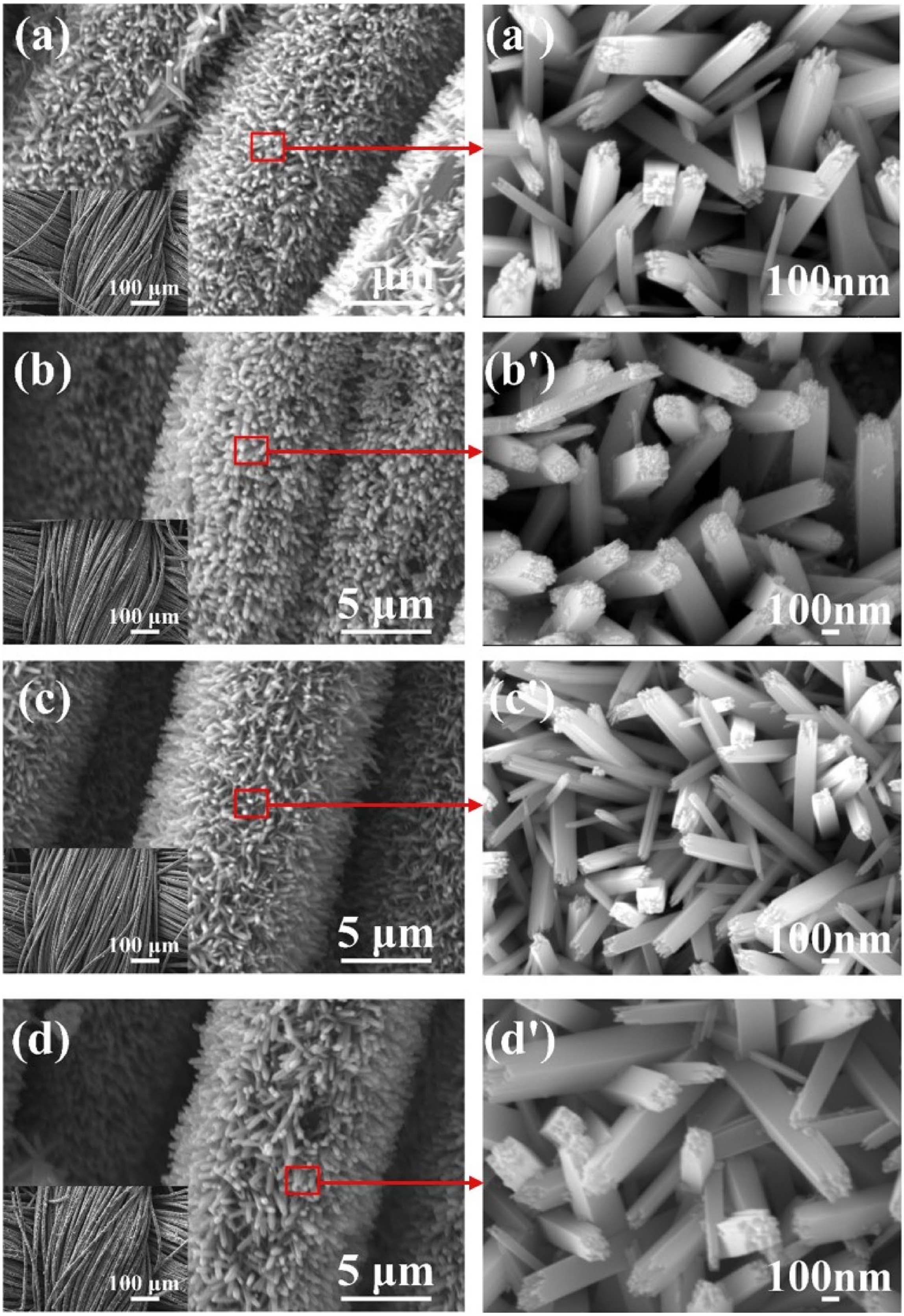

Fig. 2 SEM images of T@CC (**a**), 2F-T@CC (**b**), 3F-T@CC (**c**), and 4F-T@CC (**d**)

XPS Ti 2p spectra (Fig. 4a) for T@CC showed the doublet peak of $2p_{3/2}$ and $2p_{1/2}$ located at 457.5 and 463.2 eV, respectively. After fluorine doping, the Ti 2p peaks for 3F-T@CC shifted slightly to the lower binding energy. This can be attributed to the formation of oxygen vacancies by fluorine intercalation. XPS O 1 s spectra (Fig. 4b) can be fitted to Ti–O, O_2 and H_2O, locating at 531.4, 530.3 and 528.8 eV, respectively. After fluorine doping, the binding energy shifts to low binding energy by 0.3 eV. XPS F 1 s spectrum for 3F-T@CC (Fig. 4c) showed that F 1 s peak appeared at 683.3 eV, which is attributed to F^- in F–Ti bond and confirmed that F was successfully doped in TiO_2 nanorods. The Ti:O atomic ratio of T@CC is 33.4:66.6; while the Ti:O:F ratio of 3F-T@CC is 32.9%:66.0%:1.1%. The oxygen concentration reduces after fluorine doping. The presence of fluorine in the lattice of TiO_2 induces the formation of reduced Ti^{3+} centers, and oxygen vacancies are likely to coexist with the Ti^{3+} ions.

To evaluate the photocatalytic removal of formaldehyde, the formaldehyde concentration at the inlet (CH1) and outlet (CH2) of reactor was monitored in real time. Under 365 nm LED irradiation with intensity of 1.5 W, the formaldehyde degradation performance is shown in Fig. 5a. The inlet concentration (CH1) is set at 0.5 mg/m^3, and the formaldehyde reached the adsorption desorption equilibrium before turning on the light. When light is turned on, the formaldehyde degradation rate increases rapidly to a saturated value, then decreases slowly with the irradiation time. The evaluation of degradation performance should include the saturation value, duration at saturation. All catalysts can reach the saturation of 100% degradation of formaldehyde under 365 nm LED irradiation. The duration of 100% degradation of formaldehyde was 30 min, 30 min, 240 min, 138 min, for T@CC, 2F-C@CC, 3F-T@CC, and 4F-T@CC, respectively. At the radiation time of 240 min, the degradation rate was 74%, 82%, 100%, 96%, for T@CC, 2F-T@CC, 3F-T@CC, 4F-T@CC, respectively. Figure 5b shows stability test for 3F-T@CC. The duration of 100% formaldehyde degradation was up to 58.2 h, which is 291 times of that of T@CC.

The formaldehyde degradation performance under 420 nm LED irradiation with light intensity of 1.5 W was shown in Fig. 6a. When the light was turn on, the formaldehyde degradation rate for T@CC reaches the maximum value of 52% for duration of 100 min, then decreases gradually to 48% at time of 240 min; 2F-T@CC reaches the maximum degradation rate of 68%, then decreases gradually to 46% at time of 240 min; 3F-T@CC reaches the maximum degradation rate of 96% at time of 188.6 min and then decreases slightly to 94% at 240 min; 4F-T@CC reaches the maximum degradation rate of 84% at 14.3 min and then decreases to 76% at 240 min. The results showed that F doping increased the degradation rate for rutile TiO_2, and 3F-T@CC exhibits the best performance for formaldehyde degradation among all catalysts. Figure 6b showed the stability test of 3F-T@CC, and the formaldehyde degradation rate reached 100% after 1.7 h irradiation and lasted for 12.1 h. The photocatalytic degradation measurements demonstrated that 3F-T@CC exhibits the best performance under 365 nm and 420 nm LED irradiation.

Electron impendence spectra (EIS) (Fig. 7a) showed the corresponding interface reaction impedances (RCT) are 111.0, 91.9, 79.1 and 97.6 Ω, for T@CC, 2F-T@CC, 3F-T@CC, 4F-T@CC, respectively, indicating that the doping of

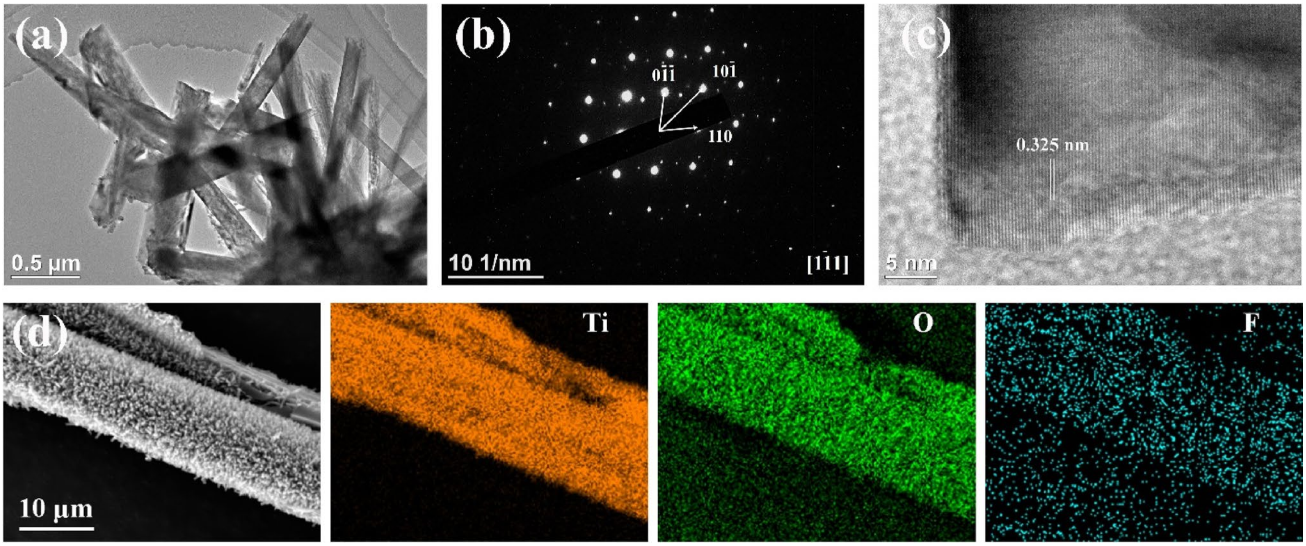

Fig. 3 TEM image (**a**), SAED pattern (**b**) and HRTEM image (**c**) of 3F-T@CC. SEM image (**d**) and EDS element mapping of Ti (**e**), O (**f**), and F (**g**) of 3F-T@CC

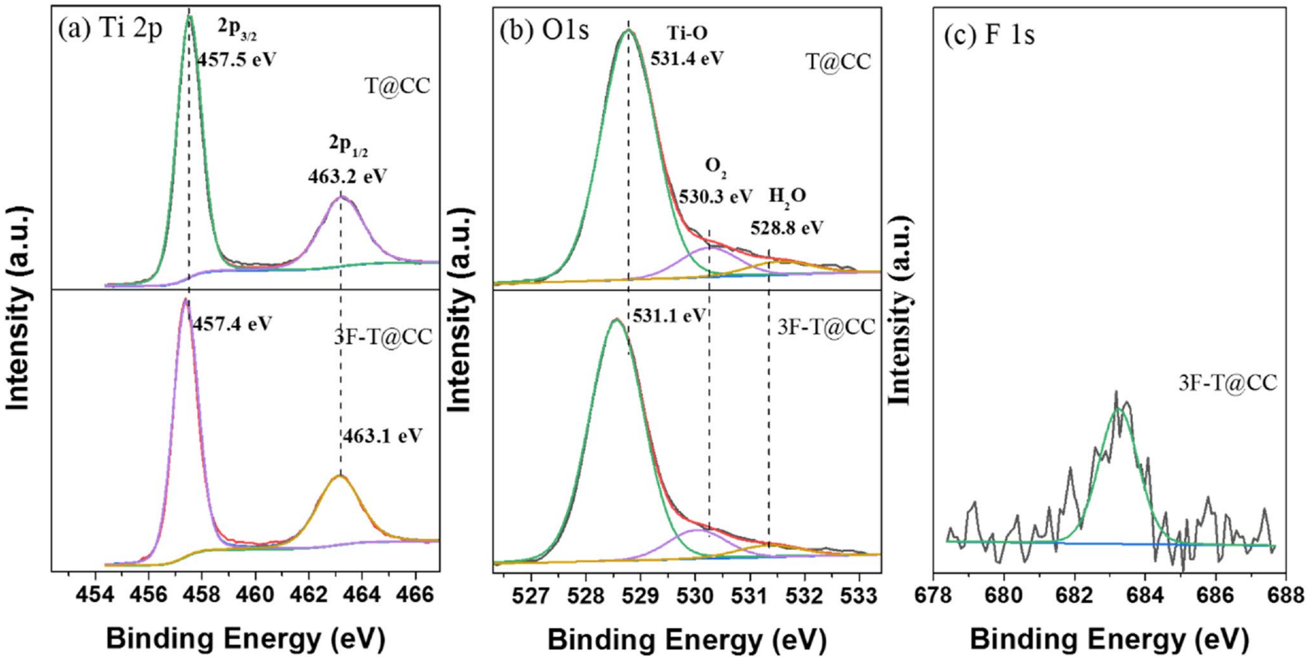

Fig. 4 Ti 2p (**a**), O 1s (**b**), and F 1s (**c**) core level XPS spectra of T@CC, and 3F-T@CC

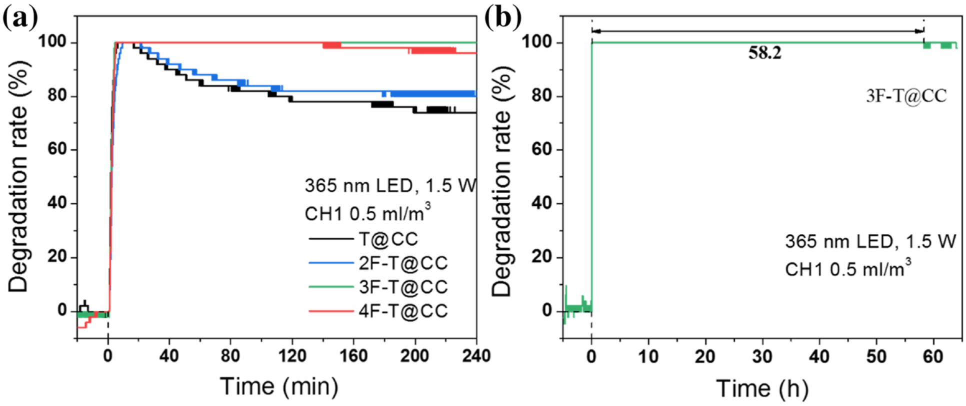

Fig. 5 HCHO degradation rate (**a**) of T@CC, 2F-T@CC, 3F-T@CC, and 4F-T@CC

F element can reduce the interface reaction impedance and facilitate the transmission of photogenerated carriers. The interface reaction impedance for 3FT@CC is the smallest. Photoluminescence spectra (Fig. 7b) showed 3F-T@CC has the lowest peak intensity, which indicates that photogenerated electron hole pairs are more effective than other samples. PL spectra of TiO_2 are attributed to three kinds of physical origins: self-trapped excitons, oxygen vacancies (OVs), and surface states. The peak at 390.3 nm is attributed to the oxygen vacancies with two trapped electrons, F center, and peak at 413.8 nm is assigned to the oxygen vacancies with one trapped electrons, F^+ center. Peak at 443.2 nm might be the lattice ions surrounding the vacancy. Peak at 466.2 nm may be caused by the defects on the surface of TiO_2 nanorods [35–38].

The UV–vis diffuse reflectance spectra (Fig. 8a) showed that F doping leads to an increase in the adsorption over ultraviolet–visible range with wavelength up to 550 nm, and the adsorption edge exhibits slight red shift. From the Tauc plot in Fig. 8b, the band gap of 3F-T@CC and 4F-T@CC is determined to be 3.01 eV, which is almost identical to that of T@CC. Apparent tail between 2.95 eV and 3.00 eV in the Tauc plot favors the light absorbance. The visible light response mainly originated from the presence of oxygen vacancies created by the fluorine doping. The valence band energy was determined from ultraviolet photoelectron spectroscopy (UPS) by subtracting the width of He I UPS spectra (Fig. 8c) from the excitation energy of 21.22 eV. The valence band energy is 7.49 eV, 7.22 eV, 6.90 eV, and 7.05 eV, for T@CC, 2F-T@CC, 3F-T@CC, and 4F-T@CC,

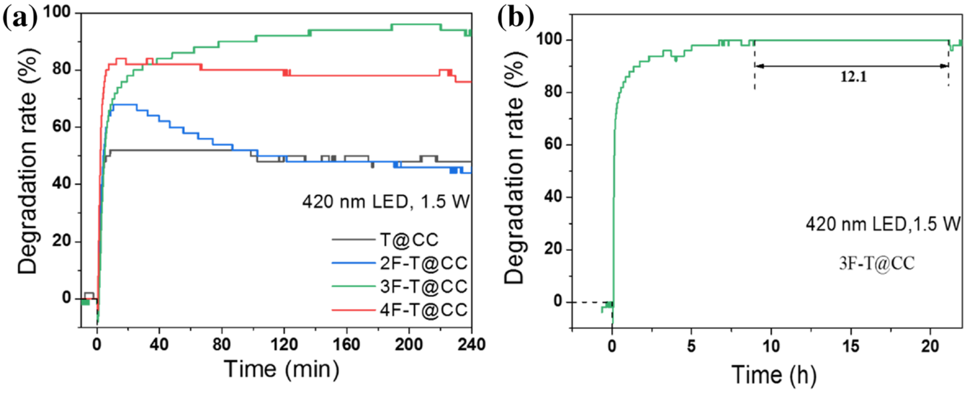

Fig. 6 HCHO degradation rate (**a**) of T@CC, 2F-T@CC, 3F-T@CC, and 4F-T@CC

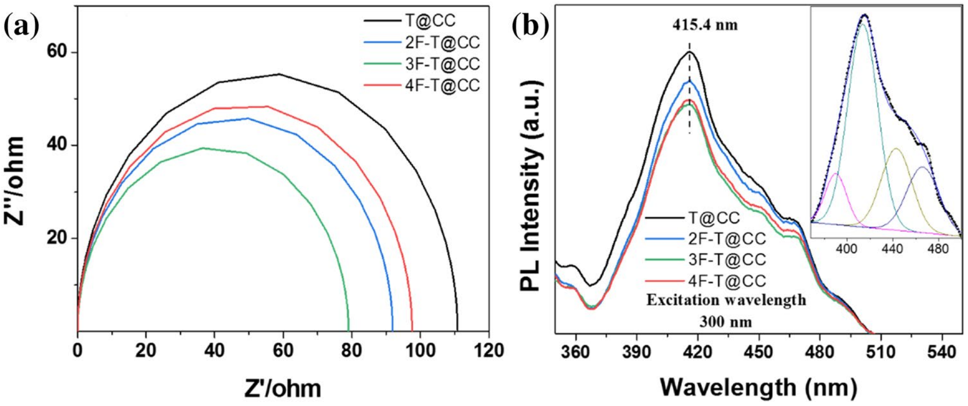

Fig. 7 Electron impendence spectra (**a**), and PL spectra (**b**) of T@CC, 2F-T@CC, 3F-T@CC, and 4F-T@CC

respectively. The valence band in electron volts is converted to electrochemical potential in volts according to the reference standard for which 0 V versus reversible hydrogen electrode (RHE) equals −4.5 eV versus vacuum level. The valence band related to RHE is 3.0, 2.7, 2.4 and 2.6 V, for T@CC, 2F-T@CC, 3F-T@CC, 4F-T@CC, respectively. Figure 8d shows the energy band structure diagram of T@CC and F doped TiO_2 system. The up-shifting the band edges should play a crucial role in the photocatalytic process. The more negative of conduction band make the photogenerated electrons to react with oxygen to generate superoxide ions ($O_2 + e^-_{CB} \rightarrow \cdot O_2^-$). Holes in valence band react with surface adsorbed water to generate hydroxyl radical ($H_2O + h^+_{VB} \rightarrow \cdot OH + H^+$) [39].

DMPO (5,5-dimethyl-1-pyrrole *N*-oxide) was used as a free radical trapping agent in EPR analysis to detect free radical intermediates ($\cdot OH$ and $\cdot O_2^-$) generated under specific potential. Upon 365 nm LED irradiation, the 3F-T@CC in the methanol dispersion system show obvious 1:1:1:1 peaks corresponding to $\cdot O_2^-$, and in the water dispersion system 1:2:2:1 peaks corresponding to $\cdot OH$, as shown in Fig. 9. The experimental results proved that the photoinduced electron–hole pairs react with adsorbed H_2O and O_2 to form $\cdot OH$ and $\cdot O_2^-$ [39–41]. The catalyst 3F-T@CC exhibits stronger signal for $\cdot OH$ and $\cdot O_2^-$ than T@CC, which confirms that fluorine doping promotes the generation of active species for photocatalytic oxidation of formaldehyde. These two kinds of free radicals have strong oxidation properties and involved in oxidize formaldehyde to CO_2 and H_2O [17].

4 Conclusions

In conclusion, rutile TiO_2 nanorod arrays were successfully grown on carbon fibers by seed assisted hydrothermal method, and the carbon fibers facilitated the transfer of photoinduced charges, while the antler-like arrays increase the active sites. The doping of F element induces oxygen vacancies, enhancing light response and tuning energy band structure. 3F-T@CC catalyst has the best photocatalytic degradation performance of formaldehyde. Under 365 nm LED irradiation, the 3F-T@CC catalyst can eliminate formaldehyde completely with duration of 58.2 h, which is 291 times of that of pure TiO_2 (0.2 h). Under 420 nm LED, the degradation rate of 3F-T@CC reached to 96% at 240 min, which is about as two times as that of pure T@CC (48%), and the duration of complete degradation reached 12.1 h. Photoinduced electron–hole pairs react with H_2O and O_2 to form $\cdot OH$ and $\cdot O_2^-$, which oxidize formaldehyde to CO_2 and H_2O. This study provide a pathway to fabricate TiO_2 arrays

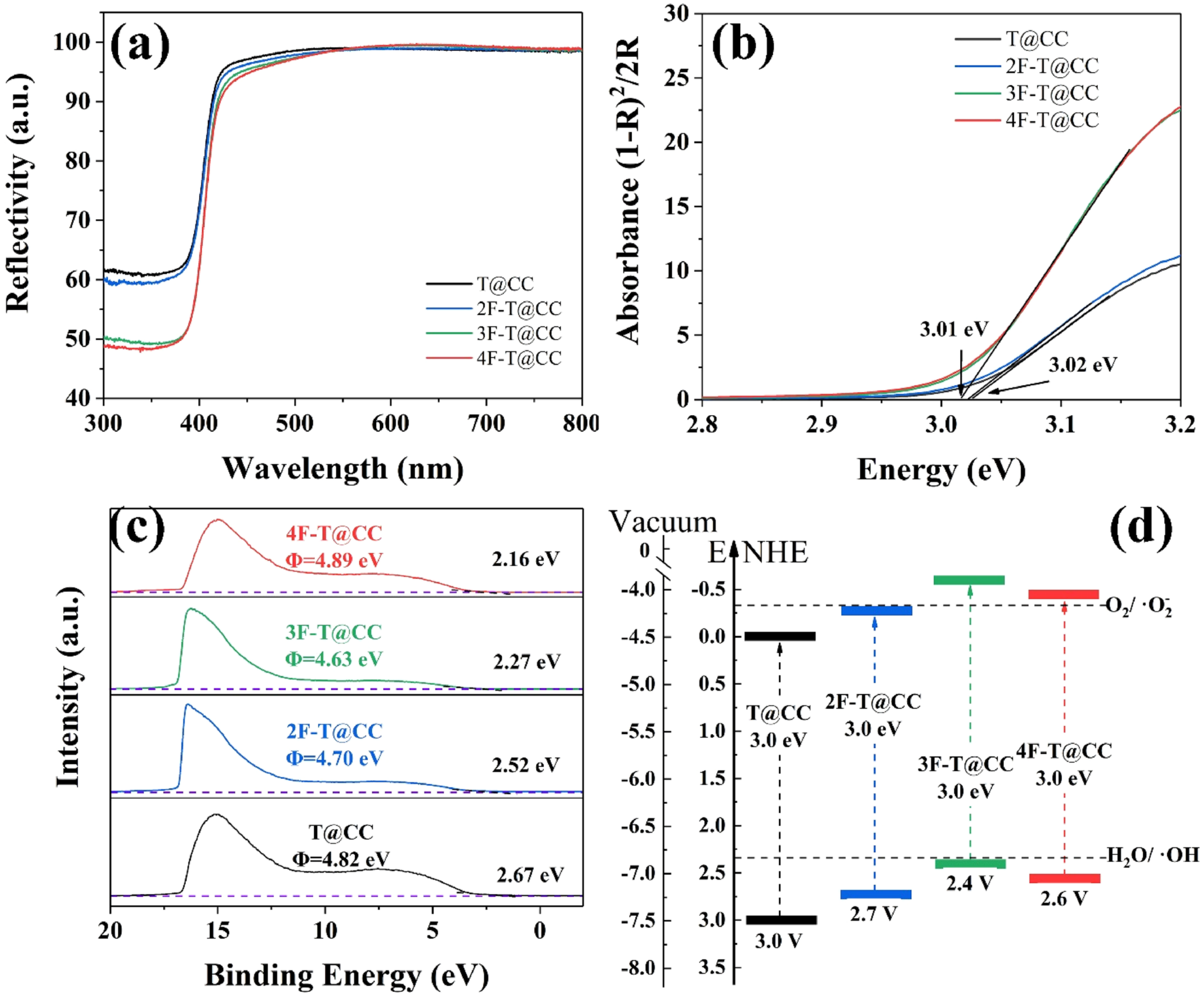

Fig. 8 UV–vis diffuse reflectance spectra (**a**) and converted Kubelka–Munk plots (**b**), UPS spectra (**c**) and schematic band structure (**d**) of T@CC, 2F-T@CC, 3F-T@CC, and 4F-T@CC

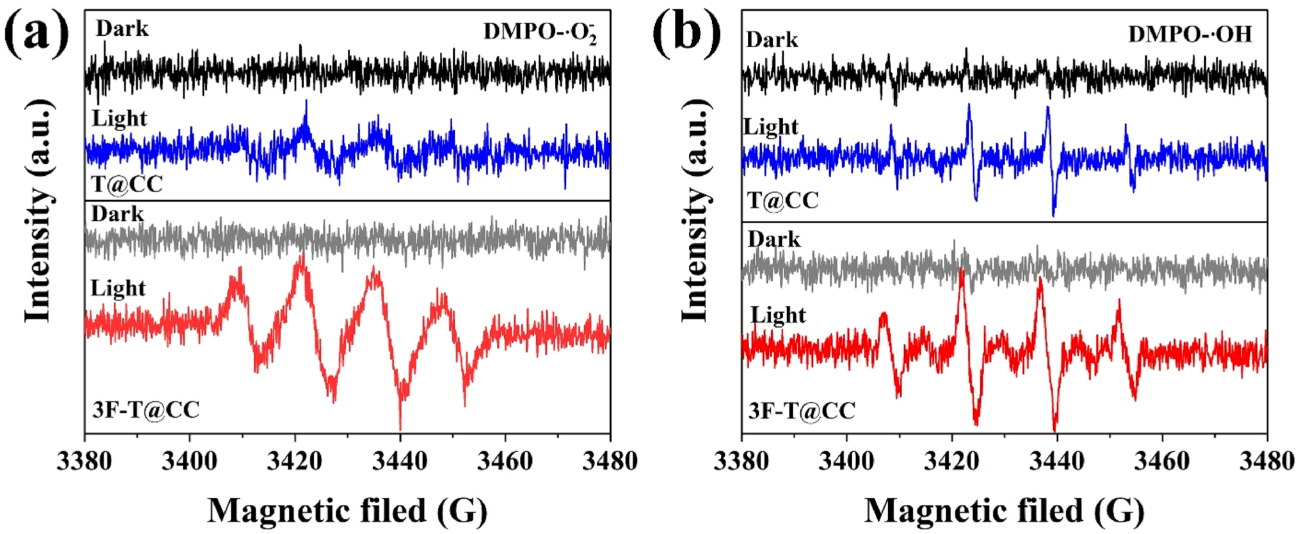

Fig. 9 EPR spectra in a methanol dispersion for DMPO-·O_2^- (**a**), and in an aqueous dispersion for DMPO-·OH (**b**) of 3F-T@CC

attached on carbon cloth at low temperature, ready for the applicable air purifier to remove formaldehyde.

Supplementary Information The online version contains supplementary material available at https://doi.org/10.1007/s10562-021-03700-x.

Acknowledgements This work was supported by the National Natural Science Foundation of China (51801164), Fundamental Research Funds for Central Universities (XDJK2020C005), Venture & Innovation Support Program for Chongqing Overseas Returnees (cx2018080).

Author Contributions The manuscript was written through contributions of all authors. All authors have given approval to the final version of the manuscript.

References

1. Yang C, Miao G, Pi Y, Xia Q, Wu J, Li Z, Xiao J (2019) Abatement of various types of VOCs by adsorption/catalytic oxidation: a review. Chem Eng J 370:1128–1153
2. He C, Cheng J, Zhang X, Douthwaite M, Pattisson S, Hao Z (2019) Recent advances in the catalytic oxidation of volatile organic compounds: a review based on pollutant sorts and sources. Chem Rev 119:4471–4568
3. Liang Q, Bao X, Sun Q, Zhang Q, Zou X, Huang C, Shen C, Chu Y (2020) Imaging VOC distribution in cities and tracing VOC emission sources with a novel mobile proton transfer reaction mass spectrometer. Environ Pollut. 265:114628
4. Wang H, Xiang Z, Wang L, Jing S, Lou S, Tao S, Liu J, Yu M, Li L, Lin L, Chen Y, Wiedensohler A, Chen C (2018) Emissions of volatile organic compounds (VOCs) from cooking and their speciation: a case study for Shanghai with implications for China. Sci Total Environ 621:1300–1309
5. Cao J, Wu F, Wen M, Peng J, Yang Y, Dong H (2021) Adsorption mechanism of typical VOCs on pristine and Al-modified MnO_2 monolayer. Appl Surf Sci. 539:148164
6. Zhang Z, Jiang C, Li D, Lei Y, Yao H, Zhou G, Wang K, Rao Y, Liu W, Xu C, Zhang X (2020) Micro-mesoporous activated carbon simultaneously possessing large surface area and ultra-high pore volume for efficiently adsorbing various VOCs. Carbon 170:567–579
7. Huang H, Chen C, Yang R, Yu Y, Albilali R, He C (2020) Remarkable promotion effect of lauric acid on Mn-MIL-100 for non-thermal plasma-catalytic decomposition of toluene. Appl Surf Sci 503:11
8. Mustafa MF, Fu X, Liu Y, Abbas Y, Wang H, Lu W (2018) Volatile organic compounds (VOCs) removal in non-thermal plasma double dielectric barrier discharge reactor. J Hazard Mater 347:317–324
9. Lyu J, Zhou L, Shao J, Zhou Z, Gao J, Li J, Dong Y, Wang Z (2020) Synthesis of $TiO_2/H_2Ti_3O_7$ composite with nanoscale spiny hollow hierarchical structure for photocatalytic mineralization of VOCs. Chem Eng J. 400:125927
10. Kim D, Yong K (2021) Boron doping induced charge transfer switching of a C_3N_4/ZnO photocatalyst from Z-scheme to type II to enhance photocatalytic hydrogen production. Appl. Catal. B. 282:119538
11. Diao W, Cai H, Wang L, Rao X, Zhang Y (2021) Efficient photocatalytic degradation of gas-phase formaldehyde by Pt/TiO_2 nanowires in a continuous flow reactor. ChemCatChem 12:5420–5429
12. Guo Y, Wen M, Li G, An T (2021) Recent advances in VOC elimination by catalytic oxidation technology onto various nanoparticles catalysts: a critical review. Appl. Catal. B. 281:119447
13. Wang Z, Yu H, Xiao Y, Zhang L, Guo L, Zhang L, Dong X (2020) Free-standing composite films of multiple 2D nanosheets: synergetic photothermocatalysis/photocatalysis for efficient removal of formaldehyde under ambient condition. Chem Eng J 394:11
14. Singh S, Mahalingam H, Singh PK (2013) Polymer-supported titanium dioxide photocatalysts for environmental remediation: a review. Appl Catal A 462–463:178–195
15. Habibi-Yangjeh A, Asadzadeh-Khaneghah S, Feizpoor S, Rouhi A (2020) Review on heterogeneous photocatalytic disinfection of

waterborne, airborne, and foodborne viruses: can we win against phthogenic viruses? J Colloid Interface Sci 580:503–514

16. Akhundi A, Habibi-Yangjeh A, Abitorabi M, Pouran SR (2019) Review on photocatalytic conversion of carbon dioxide to value-added compounds and renewable fuels by graphitic carbon nitride-based photocatalysts. Catal Rev 61:595–628
17. Dou H, Long D, Rao X, Zhang Y, Qin Y, Pan F, Wu K (2019) Photocatalytic degradation kinetics of gaseous formaldehyde flow using TiO_2 nanowires. ACS Sustain Chem Eng 7:4456–4465
18. Zhu Z, Hong W, Chen C, Wu R (2020) Novel nanoarchitechtonics olive-like Pd/$BiVO_4$ for the degradation of gaseous formaldehyde under visible light irradiation. J Nanosci Nanotechnol 20:2689–2697
19. Li X, Qian X, An X, Huang J (2019) Preparation of a novel composite comprising biochar skeleton and “chrysanthemum” g-C_3N_4 for enhanced visible light photocatalytic degradation of formaldehyde. Appl Surf Sci 487:1262–1270
20. Jin X, Zhou X, Sun P, Lin S, Cao W, Li Z, Liu W (2019) Photocatalytic degradation of norfloxacin using N-doped TiO_2: optimization, mechanism, identification of intermediates and toxicity evaluation. Chemosphere 237:124433
21. Wang X, Wang C, Jiang W, Guo W, Wang J (2012) Sonochemical synthesis and characterization of Cl-doped TiO_2 and its application in the photodegradation of phthalate ester under visible light irradiation. Chem Eng J 189–190:288–294
22. Fadlallah MM (2017) Magnetic, electronic, optical, and photocatalytic properties of nonmetal- and halogen-doped anatase TiO_2 nanotubes. Phys E 89:50–56
23. Sun H, Wang S, Ang HM, Tadé MO, Li Q (2010) Halogen element modified titanium dioxide for visible light photocatalysis. Chem Eng J 162:437–447
24. Li D, Haneda H, Labhsetwar NK, Hishita S, Ohashi N (2005) Visible-light-driven photocatalysis on fluorine-doped TiO_2 powders by the creation of surface oxygen vacancies. Chem Phys Lett 401:579–584
25. Elbanna O, Zhang P, Fujitsuka M, Majima T (2016) Facile preparation of nitrogen and fluorine codoped TiO_2 mesocrystal with visible light photocatalytic activity. Appl Catal B 192:80–87
26. Samsudin EM, Abd Hamid SB, Juan JC, Basirun WJ, Kandjani AE, Bhargava SK (2016) Effective role of trifluoroacetic (TFA) to enhance the photocatalytic activity of F-doped TiO_2 prepared by modified sol-gel method. Appl Surf Sci 365:57–68
27. Wu Y, Xing M, Tian B, Zhang J, Chen F (2010) Preparation of nitrogen and fluorine co-doped mesoporous TiO_2 and photodegradation of acid orange 7 under visible light. Chem Eng J 162:710–717
28. Dozzi MV, D’Andrea C, Ohtani B, Valentini G, Selli E (2013) Fluorinr-doped TiO_2 materials: photocatalytic activity vs time-resolved photoluminescence. J Phys Chem C 117:25586–25595
29. Dozzi MV, Artiglia L, Granozzi G, Ohtani B, Selli E (2014) Photocatalytic activity vs structural features of titanium dioxide materials singly doped or codoped with fluorine and boron. J Phys Chem C 118:25579–25589
30. Guo W, Xu C, Wang X, Wang S, Pan C, Lin C, Wang ZL (2012) Rectangular bunched rutile TiO_2 nanorod arrays grown on carbon fiber for Dye-sensitized solar cells. J Am Chem Soc 134:4437–4441
31. Diao W, He J, Wang Q, Rao X, Zhang Y (2021) K, Na and Cl co-doped TiO_2 nanorod arrays on carbon cloth for efficient photocatalytic degradation of formaldehyde under UV/visible LED irradiation. Catal Sci Technol 11:230–238
32. Hao Z, Chen Q, Dai W, Ren Y, Zhou Y, Yang J, Xie S, Shen Y, Wu J, Chen W, Xu GQ (2020) Oxygen-deficient blue TiO_2 for ultrastable and fast lithium storage. Adv Energy Mater 10:1903107
33. Mazza T, Barborini E, Piseri P, Milani P, Cattaneo D, Li Bassi A, Bottani CE, Ducati C (2007) Raman spectroscopy characterization of TiO_2 rutile nanocrystals. Phys. Rev. B 75:045416
34. Zhang Y, Harris CX, Wallenmeyer P, Murowchick J, Chen X (2013) Asymmetric lattice vibrational characteristic of rutile TiO_2 as revealed by laser power dependent Raman spectroscopy. J Phys Chem C 117:24015–24022
35. Lei Y, Zhang LD, Meng GW, Li GH, Zhang XY, Liang CH, Chen W, Wang SX (2001) Preparation and photoluminescence of highly ordered TiO_2 nanowire arrays. Appl Phys Lett 78:1125–1127
36. Howe RF, Gratzel M (1985) EPR observation of trapped electrons in colloidal TiO_2. J Phys Chem 89:4495–4499
37. Czoska AM, Livraghi S, Chiesa M, Giamello E, Agnoli S, Granozzi G, Finazzi E, Di Valentin C, Pacchioni G (2008) The nature of defects in fluorine-doped TiO_2. J Phys Chem C 112:8951–8956
38. Miyoshi A, Kuwabara A, Maeda K (2021) Effect of nitrogen/fluorine codoping on photocatalytic rutile TiO_2 crystal studied by first-principle calculations. Inorg Chem 60:2381–2389
39. Banerjee S, Pillai SC, Falaras P, O’Shea KE, Byrne JA, Dionysiou D (2014) New insight into the mechanism of visible light photocatalysis. J Phys Chem Lett 5:2543–2554
40. Nosaka Y, Nosaka A (2016) Understanding hydroxyl radical (•OH) generation processes in photocatalysis. ACS Energy Lett 1:356–359
41. Nosaka Y, Nisaka A (2017) Generation and detection of reactive oxygen species in photocatalysis. Chem Rev 117:11302–11336

Authors and Affiliations

Wenyu Diao[1] · Jiayue Xu[1] · Xi Rao[1] · Yongping Zhang[1]

✉ Xi Rao
raoxiemail@swu.edu.cn

✉ Yongping Zhang
zhangyyping@yahoo.com

[1] School of Materials and Energy, Southwest University, Chongqing 400715, China